Topical Editor: Dr. Tristan Colomb, 3D Res. **2,** 01(2011)4
10.1007/3DRes.01(2011)4

3DR REVIEW

Autofocusing in Digital Holographic Microscopy

Patrik Langehanenberg • Gert von Bally • Björn Kemper

Received: 29 September 2010 / Revised: 23 October 2010 / Accepted: 09 November 2010

Abstract Many applications in non-destructive testing at a microscopic level and in live cell imaging require automated focusing due to unstable environmental conditions, moving specimen or the limited depth of field of the applied optical imaging systems. Digital holography permits the recording and the numerical reconstruction of optical wave fields in amplitude and phase. This enables imaging of multiple focal planes from a single recorded hologram without mechanical realignment. The combination of numerical refocusing with image sharpness quantification algorithms yields subsequent autofocusing. With calibrated optical imaging systems this feature can be used also to determine the position and axial displacements of a sample. In order to show the application potential of digital holographic autofocusing in microscopy the method and results from investigations on several amplitude and phase objects are reviewed. This includes a demonstration of the reliability of automated refocusing, multi-focus quantitative phase contrast imaging of suspended cells, refocusing of quantitative phase contrast images during the analysis of the temporal dependency of cell spreading on surfaces and the quantification of toxin mediated morphological cell alterations during long-term observations. It is also shown for the example of sedimenting red blood cells that the method can be applied for minimally-invasive tracking of multiple particles. Finally, the usage of numerical autofocus for quantitative migration analysis of arbitrary shaped cells in a three-dimensional collagen matrix is demonstrated.

Keywords: digital holographic microscopy, quantitative phase contrast, multi-focus imaging, holographic autofocus, cell analysis, non destructive testing, automated 3D tracking

1. Introduction

Many applications in industrial non-destructive testing at a microscopic level and in the fields of live cell imaging require a high lateral resolution. In label-free bright field microscopy this is commonly achieved by using optical imaging systems with a high numerical aperture. However, a large numerical aperture is related to a limited depth of field. Hence, environmental conditions like temperature fluctuations, mechanical instabilities, vibrations or fast moving living specimen cause defocusing. Such focus drifts are usually compensated by realignment of the specimen or the optical imaging system. This can be performed automated by using motorized positioning hardware that is synchronized to feedback data obtained from image processing or distance measurements. Such approaches require robust and reliable procedures to determine the optimum focus position and the maximum image definition which is particularly challenging for the observation of living specimens. E. g., for long term time-lapse investigations up to several days in live cell imaging the acquisition of sharply focused images is essential as defocused images cannot be evaluated or may be misinterpreted. Furthermore, the observation of rapidly moving specimen requires a fast temporal response of autofocusing which results in expensive hardware demands.

Digital holography (DH) permits the recording and the numerical reconstruction of optical wave fields in amplitude and phase[1, 2]. In addition, by numerical propagation, subsequent refocusing from a single recorded hologram without realignment of the optical imaging system is facilitated. In microscopy DH enables high resolution lens less imaging[3-8], particle detection[9], lens based multi-focus quantitative phase contrast imaging[10-13] and the extension of the depth of focus[14-16]. Furthermore, digital holographic microscopy (DHM) has been found to be suitable for high resolution topography determination of reflective surfaces[17, 18], the inspection of optical elements (see e.g.[19]) and label-free minimally invasive dynamic analysis of transparent phase objects like living cells[11-13,20]. The combination of DH with methods for the detection of the optimum focal plane, provides autofocusing without

---

Patrik Langehanenberg[1] • Gert von Bally[1] • Björn Kemper[1](✉)
[1] Center for Biomedical Optics and Photonics, University of Muenster, Robert-Koch-Str. 45, D-48149 Muenster, Germany
e-mail: bkemper@uni-muenster.de

mechanical realignment and electronic synchronization. For example in[16] and[21] phase data is evaluated to obtain a feedback for refocusing of technical specimens. In[22-27] the reconstructed amplitude distributions or the spectral content of the object images are numerically analyzed to retrieve the optimum propagation parameters for sharply focused images. In combination with calibrated imaging systems it is also possible to determine the axial position and relative axial displacements of particles and biological specimens from a single recorded hologram[15, 28-30]. The aim of this paper is to review and demonstrate the application potentials of digital holographic autofocusing in microscopy. For this purpose, after a brief introduction to DHM, principles for digital holographic autofocusing of amplitude and phase objects are described. Afterwards, an overview of application examples is given. This includes results from investigations on the reliability of holographic autofocusing and multi-focus quantitative phase contrast imaging of suspended cells. Furthermore, automated refocusing of quantitative phase contrast images during the digital holographic analysis of the temporal dependency of cell spreading on surfaces and the evaluation of data from long-term time-lapse investigations on the quantification of toxin mediated morphological cell alterations are presented. Finally, it is shown that holographic autofocusing can be applied for minimally-invasive three-dimensional tracking of multiple sedimenting particles and to quantify the migration of arbitrarily shaped cells in a three-dimensional matrix.

2. Experimental Setups for Digital Holographic Microscopy and Numerical Evaluation of Digital Off-Axis Holograms

Fig. 1 illustrates schematically two typical setups for digital holographic microscopy[26]. Fig. 1a shows an incident light arrangement for topography measurements of reflective surfaces. Fig. 1b depicts a transmission arrangement for investigations of transparent samples, like living cells. The object under investigation is illuminated by coherent light, e. g., from a frequency-doubled Nd:YAG laser (λ = 532 nm), which is denoted as object wave (*O*). The wave that is reflected or transmitted by the sample is magnified by a microscope lens and a tube lens and imaged onto an image recording sensor, commonly a charge coupled device sensor (CCD sensor). In order to generate digital off-axis holograms the object wave is superimposed with a slightly tilted reference wave.

Various methods for the numerical reconstruction of digitally captured off-axis holograms have been developed (for an overview see e. g.[18, 31-35]). Here, the numerical reconstruction was performed by spatial phase shifting (for details see[11, 36]). The method provides the retrieval of the object wave from a single off-axis hologram without the disturbing terms twin image and zero order intensity and was found in particular suitable for robust quantitative phase contrast imaging in live cell analysis. For hologram reconstruction, in a first step an equation system is solved to retrieve the complex object wave *O* in the hologram plane. If refocusing is required, in a subsequent step, *O* is numerically propagated to the image plane. Therefore, an approach of the convolution method is applied in which the convolution theorem is applied after the Fresnel approximation[20, 38]. The advantage of this approach is that the size of the propagated wave field is preserved during the refocusing process. This is a particular advantage for numerical autofocusing as described in sections 4 to 6 as in this way the comparison of the image definition in different focal planes is simplified. In addition, the method consumes less computation time than the general approach of the convolution method[31]. However, holographic autofocusing as described in sections 4 to 6 may be applied with other common numerical propagation methods, including in particular different approaches of the convolution method[31] and the angular spectrum method[34].

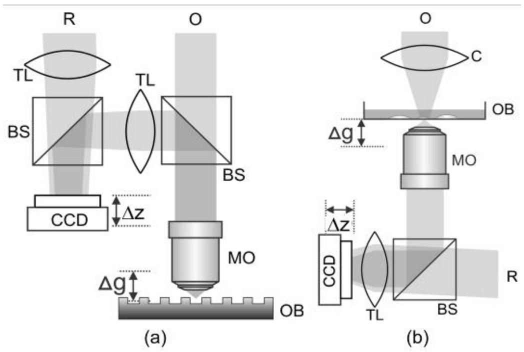

Fig. 1 Setups for digital holographic microscopy in (a) incident light and (b) transmission light arrangements. O: object wave; R: slightly tilted reference wave; C: condenser; OB: object; MO: microscope lens; BS: beam splitter; TL: tube lens; CCD: image sensor; Δz: propagation distance between the hologram and the image plane; Δg: distance between the object position and the reconstructed object plane corresponding to the hologram plane[26].

Fig. 2 illustrates the reconstruction process of a digital off-axis hologram by spatial phase shifting-based reconstruction. Fig. 2a shows a digital hologram of human red blood cells (RBCs) in phosphate buffer saline (PBS). The cells were recorded slightly defocused with a 63x microscope lens (NA=0.75) with a setup as sketched in Fig. 1b. The enlarged area in Fig. 2a shows a part of the carrier fringe pattern of the off-axis hologram that was used for holographic coding of the object wave. Fig. 2b depicts the unfocused reconstructed amplitude image of the RBCs in the CCD sensor plane. Fig. 2c displays the sharply focused amplitude after numerical refocusing. This image corresponds to a microscopic bright field image under coherent illumination. Fig. 2d shows the simultaneously obtained phase distribution modulo 2π. The resulting quantitative phase contrast image after removal to the 2π ambiguity by an unwrapping algorithm[39] is displayed in Fig. 2e. The retrieved phase contrast quantifies the delay of the optical path length that is caused by the cells in comparison with the surrounding buffer medium. Fig. 2g illustrates the cell thickness measurement along a cross-section through the phase data. The thickness of the RBC was calculated as described in[12, 37] by estimating an integral cellular refractive index n_{RBC}=1.400[40] and a refractive index n_{medium}=1.337 of the buffer solution that was obtained by an Abbe refractometer. Fig. 2g also illustrates the cell thickness by a pseudo-3D representation of the data in Fig. 2e. For completeness, Fig. 2f shows the first derivative of the data in Fig. 2d in x-direction which is comparable to

Nomarski differential interference phase contrast[41] with the additional advantages of subsequent numerical focus realignment and a variable sensitivity due to an adjustable digital shear.

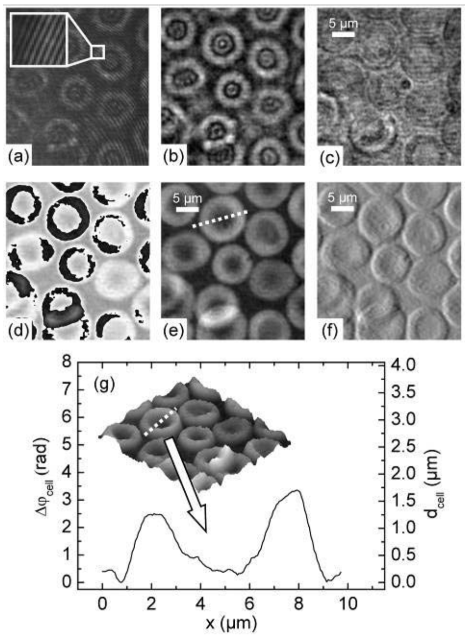

Fig. 2 Evaluation of digital holograms: (a) slightly defocused recorded digital hologram of living human red blood cells, (b): reconstructed amplitude in the hologram plane (defocused), (c): numerically refocused amplitude distribution, (d): reconstructed phase distribution modulo 2π corresponding to (c) coded to 256 gray levels; (e) unwrapped phase distribution coded to 256 gray levels; (f): first derivative of (e) in x-direction, (g): pseudo 3D representation of the phase distribution in (e) with cross section through a cell (modified from [18]).

3. Images Sharpness Quantification

Common passive optical autofocus techniques, like in compact camera photography and microscopy, are based on axial scanning of the image space by mechanical adjustment of lens elements or a stage to find the maximum image definition. In digital holography, this scanning process is performed numerically by variation of the propagation distance Δz. The main task in passive autofocusing - in digital holographic microscopy as well as in other imaging techniques - is the determination and maximization of the image sharpness. For absorbing objects (amplitude objects), e. g. with patterns that contain sharp edges, the sharply focused images contain a maximum of high spatial frequencies. Pure phase objects with negligible absorption such as technical reflective specimens or biological cells are sharply focused at the setting with the least contours in the amplitude distributions. In contrast to the bright-field case, in digital holography this setting is of particular interest, as the amplitude and phase distributions are accessible simultaneously, and the focal setting with the least-contrasted amplitude image corresponds to the best-resolved structures in the quantitative phase contrast distribution[22-24, 26]. The phase distributions obtained in the digital holographic reconstruction process contain phase jumps modulo 2π that have to be unwrapped for further evaluation. Without phase unwrapping, phase steps would be misinterpreted as sharp structures. Furthermore, in the case of unfocused reconstruction, the unwrapped phase maps may contain unwrapping errors (for illustration see Fig. 5), which also would inhibit a reliable determination of the image sharpness. Thus, for digital holographic autofocusing it is more suitable to determine of the global maximum (amplitude objects) or minimum (phase objects) of adequate focus value functions in dependence on the propagation distance Δz of the numerically reconstructed amplitude distributions. To identify a robust and time-efficient autofocus for application in digital holographic microscopy, in[26] different numerical methods that calculate a scalar focus value for the quantification of the image sharpness were compared. Therefore, common criteria to evaluate the image sharpness in bright field microscopy[42, 43] were used. In agreement with previously reported results for microscopic imaging with white light illumination[44, 45] in[24, 26] the evaluation of the weighted and band-pass-filtered power spectra

$$\text{focus value} = \sum_{\mu,\nu} \log\{1+[F_F(|O|)(\mu,\nu)]\} \qquad (1)$$

was identified to be most suitable for a robust determination of the image sharpness in digital holographic microscopy in combination with the convolution method described in section 2. In Eq. (1), (x, y) are the coordinates in spatial domain while (μ,ν) denote the corresponding spatial frequencies. The parameter $F_F(|O|)(\mu,\nu)$ denotes the band-pass-filtered Fourier Transform of the amplitude distribution $|O(x, y)|$. Logarithmic weighting is applied in order to consider also weak parts of the spatial frequency spectrum. The lower boundary of the band-pass-filter is chosen in such a way that the constant background intensity is excluded. To minimize the computation time as maximum spatial frequency the value is selected that is given by the resolution of the optical imaging system. The following sections illustrate in overview the performance and application of this method in DHM.

4. Autofocusing of Amplitude Objects

The practical application of digital holographic autofocusing by weighted spectral analysis on amplitude objects is illustrated by results from investigations on a transparent USAF 1951 resolution test chart with absorbing test structures. The investigations were performed with an experimental setup as shown in Fig. 1b (λ = 532 nm, 20x microscope lens NA=0.4). A digital hologram of the defocused test chart was recorded. After the numerical reconstruction as described in section 2, the complex object wave was propagated within the range Δz = [-15 cm; +15 cm] in steps of 0.1 cm. For each Δz, by application of Eq. 1, a focus value of the reconstructed amplitude distribution was determined. The border areas of the reconstructed amplitude and phase distributions were affected by propagation induced diffraction artifacts (see Fig. 3c). Hence, in order to investigate the influence of spatial filtering, the focus values were also calculated after application of a Hann-filter on the same reconstructed amplitude distributions. In Figs. 3a, 3b, 3c the obtained amplitude distributions for the propagation distances Δz = (10.5-2.5) cm, $\Delta z = \Delta z_{IP} = \Delta z_{AF}$ = 10.5 cm and Δz =

(10.5+2.5) cm are shown. The parameter Δz_{IP} denotes the propagation distance for which the image appears sharply while Δz_{AF} is the distance that corresponds to the maximum of the focus value function. Figs. 3d, 3e, 3f show the corresponding phase distributions. In the image plane at $\Delta z = \Delta z_{IP} = 10.5$ cm the sample appears focused with sharp edges of the test chart structures. Fig. 3g depicts the obtained normalized focus values that have been obtained by Eq. 1 in dependence of Δz in comparison to the results from the corresponding Hann-filtered data. The focus value curve of the unfiltered amplitudes shows a peak at $\Delta z = 0.0$ cm although this results in an unfocused image of the test chart. At $\Delta z = \Delta z_{IP} = 10.5$ cm, where the sharply focused image occurs (Figs. 3b and 3e), the focus value reaches a local maximum. The application of the Hann-filter prior the determination of the focus value suppresses the peak at $\Delta z = 0.0$. Thus, a non-ambiguous automated detection of the sharply focused image plane at $\Delta z = \Delta z_{IP} = \Delta z_{AF}$ is achieved. The results in Fig. 3 show that Hann-filtering avoids misinterpretations during the retrieval of the optimum focus position and thus are required for robust digital holographic autofocusing.

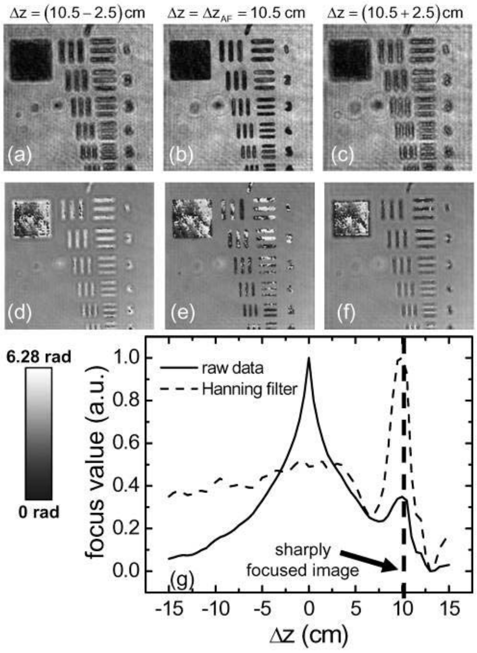

Fig. 3 Comparison of focused (b),(e) and defocused (a), (c), (d), (f) reconstructed amplitude (a)-(c) and phase distributions mod 2π (d)-(f) obtained from investigations on a USAF 1951 test chart in transmission; (g): focus values obtained by weighted spectral analysis (solid line) and by weighted spectral analysis after Hann-filtering of the amplitude distributions (dashed line) in dependence of the propagation distance Δz (modified from[24]).

5. Autofocusing of Phase Objects

The utilization of digital holographic autofocusing by weighted spectral analysis on non-absorbent phase specimen is demonstrated by results from a reflective test chart and fixed pancreas tumor cells on a glass carrier[26]. In analogy to the procedure described in section 4, a Hann-filter was applied to ensure a robust determination of the image definition. Fig. 4 shows results from investigations on a nanostructured surface (height ≈ 50 nm) in incident light arrangement as depicted in Fig. 1a (λ = 532 nm, 20x microscope lens, NA=0.4).

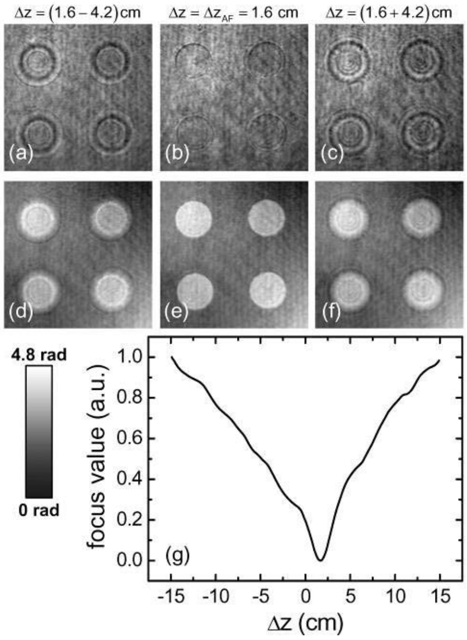

Fig. 4 Comparison of (a), (c), (d), (f) defocused and (b), (e) focused (a)-(c) reconstructed amplitude and (d)-(f) unwrapped phase distributions obtained from investigations on a nanostructured surface with incident light in reflection. (g) Focus values calculated by spectral weighted analysis in dependence of the propagation distance Δz. (modified from[26]).

Gold-coated nanostructure silicon surface, provided by the Nano+Bio Center of the Technical University of Kaiserslautern, Germany. A hologram of the slightly defocused object was recorded. Figs. 4a-4f show the impact of (de-)focusing on the reconstructed amplitudes (Figs. 4a-4c) and the unwrapped phase distributions (Figs. 4d-4f). In case of focused imaging the surface structures in the reconstructed amplitude distribution nearly disappear (Fig. 4b) while the reconstructed unwrapped phase distribution in Fig. 4e contains sharp edges. In both defocused cases the amplitude distributions show diffraction patterns and thus are visible with enhanced contrast (Figs. 4a and 4c) while the phase distributions appear blurred (Figs. 4d and 4f). In Fig. 4g the normalized focus value function obtained by spectral weighted analysis is plotted. A global minimum of the focus value is reached for $\Delta z = \Delta z_{AF} = 1.6$ cm that corresponds to the sharply focused amplitude and phase distributions of the sample. In analogy to the experiments with the reflective specimen investigations in transmission with the setup in Fig. 1b (63x microscope lens, NA=0.75) on formalin fixed pancreas tumor cells (PaTu 8988 S) on a glass carrier were carried out. This sample represents a transparent phase specimen. For hologram recording, the cells were subjectively imaged sharply onto the image sensor. The results are shown in Fig. 5. As expected from Fig. 4, the obtained focus values in Fig. 5g reach a global minimum for the sharp reconstruction at $\Delta z_{IP} = \Delta z_{AF} = 0.1$ cm. This is in agreement with the sharp appearance of the amplitude and phase distributions in Figs. 5b and 5e. The black vertical lines in the unwrapped phase distributions in Fig. 5f illustrate further, that defocusing induced diffraction patterns can lead to phase singularities and thus may cause phase-unwrapping artifacts which inhibit a further data evaluation. This illustrates also the need of digital holographic autofocusing for optimized and automated data processing in DHM which is required for time-lapse live cell imaging as described in sections 8 and 13.

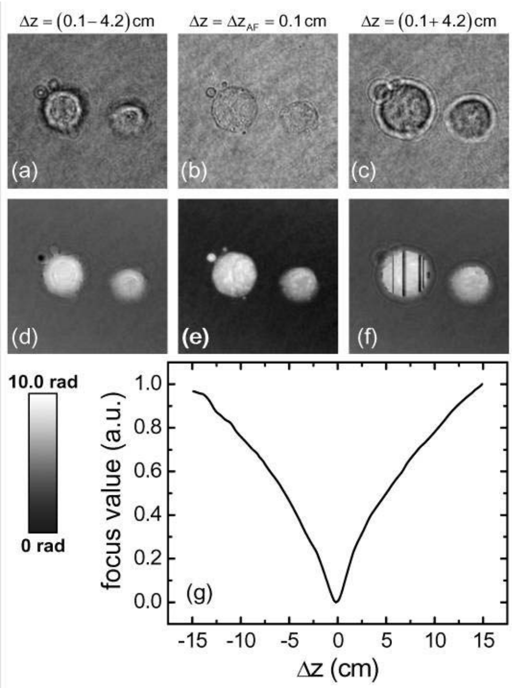

Fig. 5 Comparison of (a), (c), (d), (f) defocused and (b), (e) focused (a)-(c) reconstructed amplitude and (d)-(f) unwrapped phase distributions obtained from investigations on PaTu 8988 S cells in transmission. (g) Focus values calculated by spectral weighted analysis in dependence of the propagation distance Δz (modified from[26]).

6. Interval Search Strategy

The determination of focus value extrema within a full numerical propagation interval that typically amounts to the range Δz = [-15 cm, +15 cm] is time consuming. To accelerate the process for the localization of the optimum focus position without decrease of accuracy, an interval search strategy[24, 46] is applied. Initially, the whole propagation range of Δz is scanned with large propagation steps for the rough localization of the extremum focus value. Then, the range near the detected extremum is scanned with the smallest propagation step size with respect to the depth of field of the optical imaging system. The principle of the interval search strategy is illustrated in Fig. 6. The solid curves schematically sketch the normalized focus value functions of amplitude (Fig. 6(left)) and phase (Fig. 6(right)) objects in dependence of Δz. For amplitude objects a maximum focus value indicates the sharply focused image. Phase objects appear in the focal plane with minimum contrast and thus yield a minimum focus value. The full interval scan with a large step size is indicated by dashed vertical lines. The solid vertical lines illustrate the second scan with small steps close to the extremals. The interval search strategy is applied to accelerate digital holographic autofocusing in dynamic live cell imaging as described in sections 8-13.

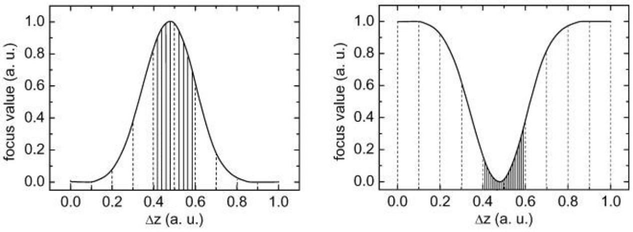

Fig. 6 Interval search strategy. Left: focus value function of amplitude objects in dependence of the propagation distance Δz; right: focus value function of phase objects in dependence of the propagation distance Δz. In a first step, the whole propagation range is scanned for the extremum focus value in large propagation steps (dashed vertical lines); in a second step, the range near the extremum focus value is scanned with the smallest step size with respect to the depth of field of the applied optical imaging system (solid vertical lines).

7. Autofocus Reliability and Axial Sample Localization

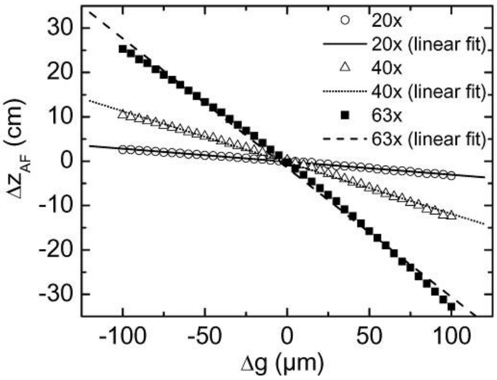

Fig. 7 Dependence of the axial object position Δg on the autofocus distance Δz_{AF} for three different microscope lenses (Zeiss LD Achroplan 20x/0.4 Korr, Zeiss APlan 40x/0.65, Zeiss LD Plan-Neofluar 63x/0.75 Korr), each in comparison to a linear fit.

The relation between the distance Δg of the object to the focal plane and the propagation distance Δz to the image plane can be used to quantify relative axial object displacements without mechanical focus realignment. In case of insufficient data about optical imaging system components, e. g., if DHM is applied with research microscopes as described in[47], the conversion between Δz and Δg may not analytically be derived. Instead, a calibration via the digital holographic autofocus approach can be used to obtain the dependency between Δz and Δg. The calibration procedure is performed by recording a set of stepwise defocused digital holograms of a sample[26]. Therefore, the relative object position Δg is varied in axial direction, e. g., with a calibrated microscope stage, while Δz_{AF} is determined by subsequent digital holographic autofocusing as previously described in sections 4 to 6. Fig. 7 shows the autofocus propagation distances Δz_{AF} for three different microscope lenses (20x, 40x, 63x) in dependence of Δg. The results were experimentally obtained by investigations on fixed pancreas tumor cells (for illustration see Fig. 5) in transmission with the experimental setup depicted in Fig. 1b. The experimental data are found to be in good agreement with a linear approximation and demonstrate the reliability of digital holographic autofocus. The linearity coefficients between Δg and Δz_{AF} for the applied imaging systems are determined to (-0.029±0.001) cm/µm (20x), (-0.116±0.001) cm/µm (40x) and (-0.291±0.003) cm/µm (63x) and are specific for the imaging properties of the used experimental setup. The slight deviations of the experimental data from fitted curves for propagation distances |Δz| > 50 cm - in particular for the 63x lens - result from the slightly changing magnification due to the different object positions that is not considered by the linear approximation. The maximum resolution for the detection of relative axial displacements depends on the depth of field and thus on the numerical aperture and magnification of the applied microscope.

8. Subsequent Multi Focus Imaging

DH enables the reconstruction of different focal planes from a single hologram. This multi-focus imaging feature is particularly suitable for investigations of particles and cells in suspension as several specimens in different planes can be recorded simultaneously. Furthermore, in combination with numerical autofocusing the determination of relative object positions in z-direction is provided. Fig. 8 illustrates quantitative digital holographic multi-focus imaging by results from pancreas tumor cells in suspension. Therefore, living trypsinized PaTu 8988 S cells in cell culture medium (DMEM) were investigated using the inverted digital holographic microscopy setup sketched in Fig. 1b (λ = 532 nm, 63x microscope lens, NA = 0.75,). Fig. 8a shows a digital off-axis hologram of three cells. The diffraction patterns indicate that the cells denoted as A, B and C were located in different planes. For the numerical reconstruction in a region of interest (ROI) around each cell the maximum image definition was determined by calculation of a focus value in dependence of the propagation distance Δz with Eq. 1. Figs. 8b-8d show the amplitude distributions obtained by application of numerical autofocusing in the three ROIs around each cell that are marked with boxes. In each ROI one of the cells appears sharply focused with minimum contrast (autofocus criterion). Figs. 8e to 8g show the corresponding unwrapped quantitative phase contrast images of the cells and illustrate the requirement for precise subsequent numerical focus correction. The phase distributions caused by the unfocused imaged cells contain unwrapping artifacts that prevent a further data evaluation. In contrast, the sharply imaged samples appear clearly resolved and deliver qualitative data with minimized unwrapping errors. In Fig. 8h the focus values are plotted for each ROI in dependence of the propagation distance Δz. The corresponding distance Δg in object space is obtained by calibration the imaging system as described in section 5. The minima of the curves (cell A: Δz_{AF} = 5.8 cm, cell B: Δz_{AF} = 0.8 cm, cell C: Δz_{AF} = 1.0 cm) indicate the propagation distances for the sharply focused imaging of each cells and are in agreement with the appearance to the amplitude and phase distributions in Figs. 8b-8g. The relative axial distance of the cells in z-direction are: A:B ≈ 17 µm, A:C ≈ 23 µm, B:C ≈ 6 µm. Finally, Fig. 8i shows the phase distribution results from merging the sharply focused images of the cells in Figs. 8e-8g in which all cells appear sharply focused. The results show that for an optimized imaging of cells in suspension numerical multi-focus imaging is required. The minimal error for the detection of the axial sample position is restricted by the depth of field of the applied microscope lens (here: ≈ 0.4 µm). In practice the precision is decreased by the shape of the investigated specimen and the noise in the reconstructed amplitude distributions that depend on the individual measurement conditions. Thus, for the described experiment the error for the determination of relative axial positions can be estimated to be in the range of ≈ 2 µm.

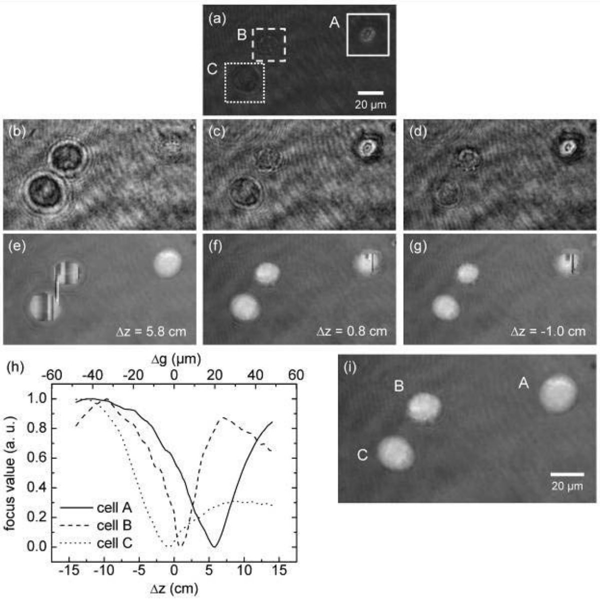

Fig. 8 Subsequent multi-focus imaging of cells in suspension. (a): digital hologram of three pancreas tumor cells (PaTu 8988 S) in different focal planes denoted as A, B, C; (b),(c),(d): amplitude distributions of the cells for different propagation distances obtained by numerical autofocusing in the region of interests (ROIs) marked with boxes, (e),(f), (g): gray level coded unwrapped phase contrast images corresponding to (b),(c),(d). (h): focus values in dependence of the propagation distance Δz and the corresponding distance Δg in object space in the areas marked with boxes, (i): enlarged phase distribution merged from the sharply focused parts in (e),(f),(g). The minima of the curves in (h) indicate the propagation distances for the sharply focused imaging of the cells.

9. Analysis of Cell Adherence on Surfaces

The quantitative analysis of cell adherence is important for the characterization of cellular interactions with different surfaces and surface coatings. Here, the usage of DHM in combination with subsequent numerical autofocusing for dynamic analysis of cell adherence processes is demonstrated by results from the observation of the spreading process of a living keratinocyte cell on a glass carrier. For the experiments a DHM setup as depicted in Fig. 1b was used (λ = 532 nm, 40x microscope lens, NA=0.6. At the beginning of the experiment the sample was manually focused sharply onto the image recording device. Digital off-axis holograms of the cell were recorded with fixed mechanical focus every 5 s over a period of 16 min in a temperature stabilized environment (T = 37 °C). The reconstruction of the resulting 192 holograms was performed as explained in section 2. Due to the fixed alignment of the optical imaging system the cell moves out of focus during the experiment. Thus, the hologram reconstruction was carried out in combination with numerical autofocusing as described in sections 5 and 6. In order to analyze the influence of the autofocus procedure the resulting amplitude and phase contrast images were compared to data that were obtained without autofocusing.

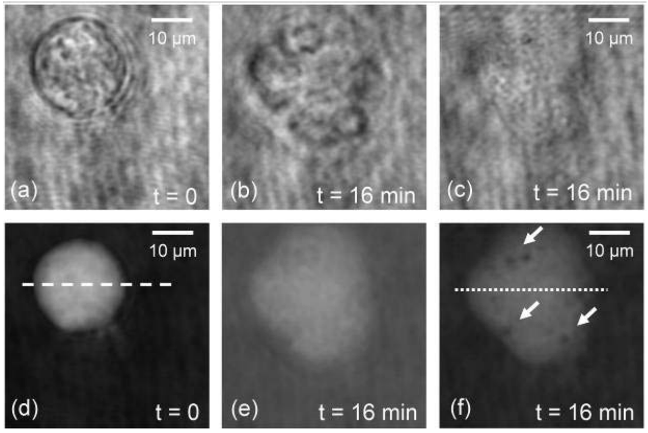

Fig. 9 DHM investigations on a spreading keratinocyte cell (40x microscope lens, NA=0.6). Upper row: amplitude distribution; lower row: phase contrast images; (a), (d): t = 0, (b), (e): t = 16 min without numerical autofocusing; (c), (f): t = 16 min with numerical autofocusing. In (f) subcellular structures become visible that are marked with arrows (modified from[24]).

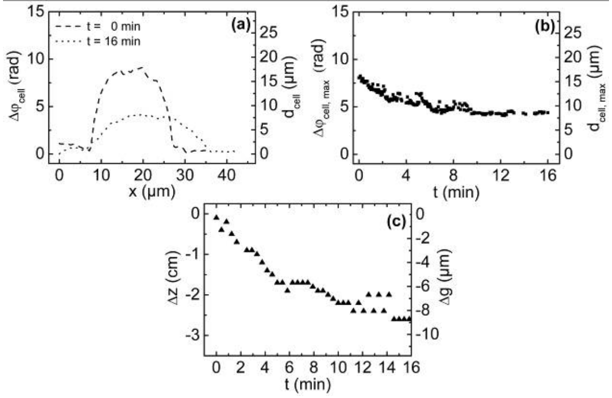

Fig. 10 DHM investigations on a spreading keratinocyte cell. (a): cross-sections through the phase data marked with dashed and dotted lines in Fig. 9 and corresponding cell thickness d_{cell}. (b): temporal dependence of the maximum phase contrast $d_{cell;max}$ and maximum cell thickness $d_{cell;max}$. (c): Temporal dependence of the autofocus propagation distance Δz_{AF} and the corresponding relative displacement of the sample Δg in object space (illustrated for 40 of 192 holograms) (modified from[50]).

Fig. 9 shows representative examples for amplitude and phase contrast images. Figs. 9a and 9d depict the results for t = 0. As the sample is imaged sharply at the initiation of the experiment no numerical refocusing is performed (propagation distance: $\Delta z = 0$). The cell appears sharply and almost spherical in both, amplitude and phase contrast images. Figs. 9b and 9e depict the amplitude and phase distributions that are achieved with the same reconstruction parameters for t = 16 min. Diffraction patterns in the amplitude images indicate that the cell moved out of focus and the phase contrast image of the cell appears blurred. Figs. 9c and 9f present the images that are retrieved from the same hologram after numerical autofocusing. Now the cell appears with minimum contrast in the amplitude distribution. In the corresponding phase contrast image the cell appear with clear boundaries. Furthermore, subcellular structures become visible (see dark spots in Fig. 9f that are marked with arrows) that are interpreted as vacuoles[48]. Fig. 10a shows cross-sections through the phase contrast images for t = 0 and t = 16 min that are marked with a dashed and a dotted line in Figs. 9d and 9f. The corresponding cell thickness d_{cell} depicted on the right y-axis was calculated for n_{cell} = 1.377 (obtained from suspended cells as described in[49]), and n_{medium} = 1.337. The temporal dependency of the maximum phase contrast $\Delta\varphi_{cell,max}$ as well as the corresponding maximum cell thickness $d_{cell,max}$ are plotted in Fig. 10b. For both parameters a monotone decrease up to 50% is observed. Fig. 10c displays the temporal development of the autofocus propagation distance Δz_{AF} in the image space for the evaluation of 40 of the recorded 192 holograms. The corresponding relative displacement Δg in the object space was obtained by calibration of the optical imaging system as described in section 5. The phase contrast and cell thickness decrease observed in Figs. 10a and 10b is caused by the change of the initial spherical shape of the cell to a thin layer that adheres to the substrate. The cell thickness that is calculated for the initial spherical cell corresponds to the diameter of cell in the image plane. This supports the estimated value for the integral cellular refractive that is used for the calculation of the cell thickness from the phase contrast images. The results in Fig. 9 and the continuous change of Δz_{AF} and Δg in Fig. 10 demonstrate the requirement for permanent automated focus tracking during the observation of cell spreading processes. The step-function-like temporal dependency of the autofocus distance results from the limited depth of field of the applied microscope lens (here ≈ 1.7 µm) that restricts the minimum step width of the propagation distance. In conclusion the results described in this section demonstrate that digital holographic autofocussing can be utilized for quantitative monitoring of cell adherence and cell spreading kinetics.

10. Autofocusing during Long-Term Investigations

In analogy to section 9 the application of digital holographic autofocusing for long-term-live cell imaging is illustrated by data obtained from the analysis of the reactions of living human brain micro vascular endothelia cells (HBMECs) on a toxin. The experiments were performed at 37 °C with a DHM setup as depicted in Fig. 1b using a 40x microscope lens (NA=0.6, λ = 532 nm). Figs. 11a to 11f show representatively amplitude and phase contrast images. At the beginning of the experiment (t=0) the investigated HBMECs were imaged sharply in the hologram plane (Figs. 11a and 11d). Due to a mechanical instability of the experimental setup, after t=31.5 h, without numerical focus correction the cells appeared unfocused in the reconstructed amplitude and phase distributions (Figs. 11b and 11e). The resulting images after numerical refocusing are shown in Figs. 11c and 11f. The cells appear sharply and subcellular structures are clearly resolved. Furthermore, toxin induced apoptotic effects become visible. Fig. 11g depicts the temporal dependency of the focal position that was detected by numerical autofocusing for the whole measurement period (t_{max} = 52 h). The nonlinear drift illustrates the need for a permanent focus control during long-term investigations. Furthermore, quantitative measurement data for the object position is provided that may be used to improve the stability of the experimental setup or to identify the sources of instability.

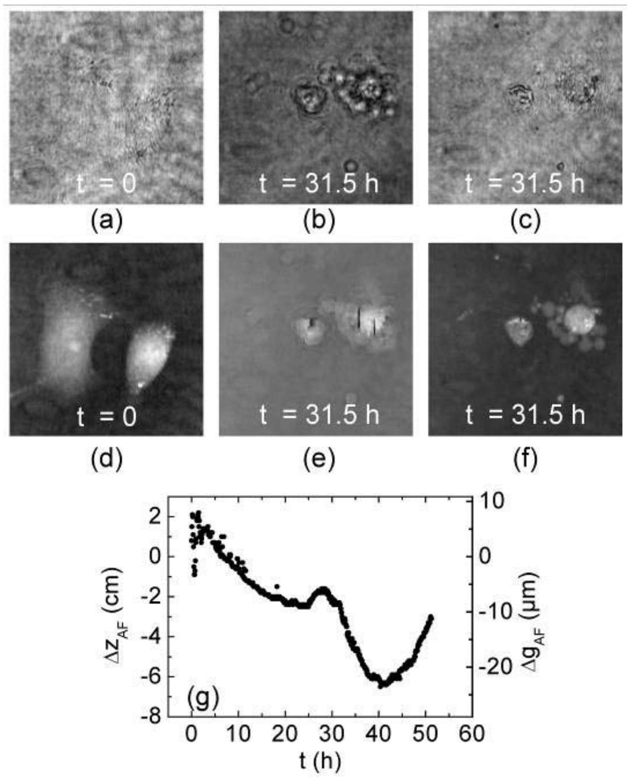

Fig. 11 Reconstructed amplitude (a)-(c) and unwrapped phase (d)-(f) distributions obtained from long-term-investigations on living HBMEC s; (a),(d) t=0, (b),(e) t=31.5 h without autofocusing, (c),(f) t=31.5 h with autofocusing, (g) time dependency of autofocus position z_{AF} and corresponding change of the axial object position ΔgAF[24].

11. Two- and Three-Dimensional Tracking of Particles and Cells

In addition to the detection of axial sample displacements as described in sections 7 and 8 from the automated refocused quantitative phase contrast images also the lateral position of a sample can be determined[30, 50-52]. Therefore, in a first step the phase distributions are low-pass-filtered with a box average filter. In this way, substructures of the object in the phase distributions and noise, e. g., due to parasitic interferences and coherent noise are reduced. Afterwards, within a ROI in which the sample is located, the pixel coordinates of the maximum phase contrast are determined. The time-dependent automated tracking of dynamic displacements from digital holograms of time-lapse sequences can be performed by successive recentering of the ROI to the coordinates of the preceding maximal phase value and reapplication of the autofocus procedure. Employing a calibrated imaging scale the resulting lateral displacement trajectories of the sample in pixel coordinates can be converted to metric units. The combination of the data with the axial object displacement Δg is obtained from the autofocus propagation distance yields quantitative 3D object tracking. In sections 12 and 13 it is demonstrated that digital holographic 3D tracking can be applied for the label-free analysis of sedimenting cells in suspension and migrating tumor cells in three-dimensional tissue models.

12. 3D-Tracking of Sendimenting Human Erythrocytes

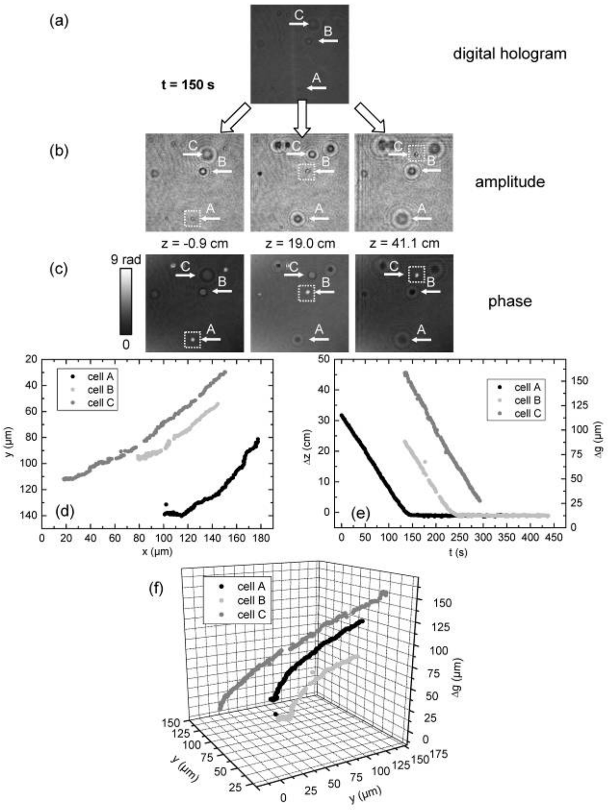

Fig. 12 Time dependent DHM 3D tracking of sedimenting human red blood cells (RBSs, spherical spiky shaped echinocytes). The tracked cells are denoted with A, B and C. (a): exemplarily digital hologram of three suspended echinocytes in different plane 150s after the begin of the experiment; (b): sharply focused amplitude distributions for each cell obtained by application of digital holographic autofocus from the hologram in (a); (c): quantitative phase distributions obtained of the digital hologram in (a); the dotted boxes in (b) and (c) represent the ROIs that are applied for digital holographic autofocus and dynamic *x*-*y*-tracking; (d): *x*-*y*-trajectory of the RBCs obtained by determination the coordinates with maximum phase contrast; (e): time dependence of the axial positions Δg of the cells obtained by digital holographic autofocusing; (f): 3D trajectories obtained by combination of the data in (d) and (e)[51].

The applicability of automated digital holographic 3D cell tracking was investigated by observation of the sedimentation process of three human red blood cells (RBCs, spherical spiky shaped echinocytes) in physiological solution. The experiments were performed with an experimental setup as shown in Fig. 1b (λ= 532 nm, 63x microscope lens, NA=0.75). A series of 438 digital holograms (Δt = 1 s) was recorded at fixed optical focus. Afterwards the holograms were evaluated for 3D tracking as described in section 11. During the time dependent observation the cells perform fast dynamic motions. Thus, a permanent and robust numerical realignment of the focal position is required. Fig. 12a exemplarily depicts a digital hologram of the three echinocytes 150s after the start of the digital holographic observation. The three tracked cells are denoted with A, B and C. Fig. 12b presents sharply focused amplitude distributions obtained by application of digital holographic autofocus for each cell from the hologram in Fig. 12a. In Fig. 12c the corresponding quantitative phase distributions are depicted. The dotted boxes in Figs. 12b and 12c represent the ROIs that are applied for both, digital holographic autofocusing and dynamic *x*-*y*-tracking. Fig. 12d shows the resulting *x*-*y*-trajectories of the RBCs obtained by the determination the coordinates with maximum phase contrast. In Fig. 12e the time dependence of the axial cell positions Δ*g* is plotted. Fig. 12f shows the 3D trajectories of the cells that result from combination of the data in Figs. 12d and 12e. Figs. 12d-12f demonstrate the reliability of digital holographic 3D tracking. Nearly 100 percent of the phase contrast images have been autofocused and reconstructed without unwrapping errors. Furthermore, the sedimentation process of the RBCs due to gravitation is illustrated and quantified.

13. Monitoring of Cell Migration in a Three-Dimensional Matrix

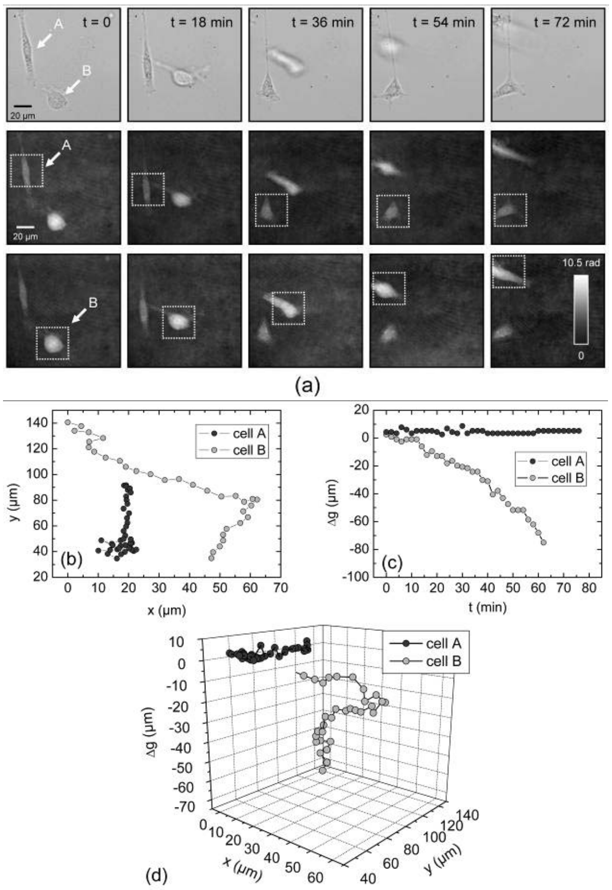

Fig. 13 (a): 3D migration monitoring of fibroblasts in collagen. First row: bright-field images (white light illumination); second row: DHM phase contrast images with 3D tracking ROI set to cell A (red boxes); third row: DHM phase contrast images with 3D tracking ROI set to cell B (green boxes). (b): lateral displacement, (c): axial displacement, (d): 3D trajectories resulting from the data in (c) and (d) (modified from[53]).

Investigations on the applicability of DHM for 3D cell migration monitoring were performed by observing two mouse fibroblasts (3T3) within a three-dimensional collagen matrix in a Petri dish with a setup as depicted in Fig. 1b (λ = 532 nm, 40x microscope lens, NA=0.65). The temperature was stabilized to 37 °C. A series of holograms and white light images was recorded with fixed mechanical focus for a period of 100 min (Δt=2 min). For both cells digital holographic 3D tracking was performed as described in section 11. Fig. 13a depicts representative results for t=0, t=18 min, t=36 min, t=54 min, and t=72 min. The first row of Fig. 13a shows bright-field images of the sample under white light illumination. The corresponding DHM phase contrast images are depicted in the second and third row of Fig. 13a. The observed cells are denoted as A and B. The dotted boxes in the phase contrast images mark the ROIs that were evaluated for 3D tracking. In the white light images, cell A only slightly moves out of. Cell B migrates to a different collagen layer and thus appears with increasing defocus during the observation. In the second row of Fig. 13a the ROI for digital holographic autofocusing was set to cell A, which appears sharply focused in the resulting quantitative phase contrasts images. In the third row of Fig. 13a the ROI was set to cell B. After digital holographic autofocusing, cell B is sharply resolved in all phase distributions. Furthermore, deformations and cell thickness changes due to the migration process become visible. The *x*-*y* migration trajectories and the corresponding temporal dependency of the axial displacements of the cells are plotted in Figs. 13b and 13c. Fig. 13d presents the 3-D migration trajectories that result from the combination of the data in Figs. 13b and 13c. Cell A moves almost in parallel to the *x*-*y*-plane. In contrast, cell B migrates to a collagen layer approximately located 65 µm below its initial position.

14. Discussion and Conclusions

The results in sections 8 to 10 and 12 to 13 demonstrate that the spectral weighted analysis of reconstructed amplitude images is capable of subsequent numerical autofocusing in digital holographic microscopy. In sections 4 it was shown that for identification of focal planes a suppression of diffraction artifacts that are caused by the numerical propagation is required. This can be efficiently achieved by a Hann-filter. Sections 4 and 5 illustrate that the method can be applied for both, amplitude and phase specimen. However, the usage of the method with mainly transparent phase objects, like reflective surfaces and living cells is of more practical advantage as in addition to the image of the sample also quantitative phase contrast is provided that can be evaluated for quantitative measurements. For example, automated numerical focusing can be used for the automation of multi-focus imaging of specimen that are located in different focal planes (section 8). This provides, e. g., an acceleration of data retrieval for the experimental determination of the integral cellular refractive index of suspended cells[30]. In addition, subsequent numerical autofocusing results in an optimized quality of the quantitative phase contrast images (see Figs. 4, 5, 8, 9 and 11). In particular, this is important for measurements that require for example a dynamic analysis of intracellular organelles. Furthermore, as demonstrated in sections 8, 12 and 13, digital holographic autofocus enables the localization of the axial sample position. It was shown that this feature provides in combination with algorithms to detect lateral displacements in quantitative DHM phase contrast images 3D tracking of particles and cells even with an arbitrary shape.

The results from Fig. 7 and from the time dependent measurements in Figs. 10 to 13 demonstrate the robustness and reliability of the proposed method for autofocusing. However, the measurement accuracy of the detection of the optimum focus and the corresponding axial sample position depends on the depth of field of the used imaging system and the shape of the investigated object. The main error sources for autofocusing are scattering effects that are caused by the medium in which the sample is investigated, the scattering properties of the sample itself and coherent noise. Thus, in practice the typical accuracy for the detection of axial displacements can be estimated to be in the range of 1-2 µm. Furthermore, it has to be mentioned that due to the underlying principles of the presented DHM configurations integral information is obtained. Thus, specimens in different planes at the same lateral position with axial distances near the DOF of the applied imaging system cause diffraction patterns. This can lead to misinterpretations in the image sharpness quantification process. Furthermore, these disturbances affect the correct determination of the lateral object position from the quantitative phase contrast images. This limits the density of objects under investigations to an amount in which the specimen are imaged laterally separated. Nevertheless, numerical autofocusing and its usage to obtain axial data for 3D tracking in DHM prospects new application areas of quantitative digital holographic phase contrast imaging for particle tracking in fluidics and label-free 3D migration analysis of cells in cancer research.

Acknowledgements

Support by the German Federal Ministry for Education and Research (BMBF) and the European Network of Excellence “Nano2Life” is gratefully acknowledged.

References

1. J. W. Goodmann, R. W. Lawrence (1967) Digital image formation from electronically detected holograms, *Appl. Phys. Lett.* **11**: 77-79
2. U. Schnars, W. Jüptner (1994) Direct recording of holograms by a CCD target and numerical reconstruction, *Appl. Opt.* **33**: 179–181
3. W. S. Haddad, D. Cullen, J. C. Solem, J. W. Longworth, A. McPherson, K. Boyer, C. K. Rhodes (1992) Fourier-transform holographic microscope, *Appl. Opt.* **31**: 4973-4978
4. E. Cuche, F. Bevilacqua, C. Depeursinge (1999) Digital holography for quantitative phase-contrast imaging, *Opt. Lett.* **24**(5): 291-93
5. Y. Takaki, H. Ohzu (1999) Fast numerical reconstruction technique for high-resolution hybrid holographic microscopy, *Appl. Opt.* **38**: 2204-2211
6. P. Pedrini, S. Schedin, H. J. Tiziani (2000) Spatial filtering in digital holographic microscopy, *J. Mod. Opt.* **47**: 1447-1454
7. W. Xu, M. H. Jericho, I. A. Meinertzhagen, H. J. Kreuzer (2001) Digital in-line holography for biological applications, *PNAS* **98**: 11301-11305
8. M. Kanka, R. Riesenberg, H. J. Kreuzer (2009) Reconstruction of high-resolution holographic microscopic images, *Opt. Lett.* **34**: 1162-1164
9. W. Yang, A. B. Kostinski, R. A. Shaw (2006) Phase signature for particle detection with digital in-line holography, *Opt. Lett.* **31**: 1399-1401
10. E. Cuche, P. Marquet, C. Depeursinge (1999) Simultaneous amplitude contrast and quantitative phase-contrast microscopy by numerical reconstruction of Fresnel off-axis holograms, *Appl. Opt.* **38**: 6694– 7001
11. D. Carl, B. Kemper, G. Wernicke, G. von Bally (2004) Parameteroptimized digital holographic microscope for high-resolution livingcell analysis, *Appl. Opt.* **43**: 6536–6544
12. P. Marquet, B. Rappaz, P. J. Magistretti, E. Cuche, Y. Emery, T. Colomb, C. Depeursinge (2005) Digital holographic microscopy: a noninvasive contrast imaging technique allowing quantitative visualization of living cells with subwavelength axial accuracy, *Opt. Lett.* **30**: 468–470
13. C. J. Mann, L. Yu, C.-M. Lo, M. K. Kim (2005) High-resolution quantitative phase-contrast microscopy by digital holography, *Opt. Express.* **13**: 8693–8698
14. P. Ferraro, S. Grilli, D. Alfieri, S. De Nicola, A. Finizio, G. Pierattini, B. Javidi, G. Coppola, V. Striano (2005) Extended focused image in microscopy by digital Holography, *Opt. Express.* **13**: 6738-6749
15. M. Antkowiak, N- Callens, C. Yourassowsky, F. Dubois (2008) Extended focused imaging of a microparticle field with digital holographic microscopy, *Opt. Lett.* **33**: 1626-1628
16. T. Colomb, N. Pavillon, J. Kühn, E. Cuche, C. Depeursinge, Y. Emery (2010) Extended depth-of-focus by digital holographic microscopy, *Opt. Lett.* **35**: 1840-1842
17. J. Kühn, T. Colomb, F. Montfort, F. Charrière, Y. Emery, E. Cuche, P. Marquet, C. Depeursinge (2007) Real-time dual-wavelength digital holographic microscopy with a single hologram acquisition, *Opt. Express.* **15**: 7231-7242
18. B. Kemper, G. von Bally (2008) Digital holographic microscopy for live cell applications and technical inspection, *Appl. Opt*. **47**: A52–A61
19. F. Charrière, J. Kühn, T. Colomb, F. Montfort, E. Cuche, Y. Emery, K. Weible, P. Marquet, C. Depeursinge (2006) Characterization of microlenses by digital holographic microscopy, *Appl. Opt*. **45**: 829–835
20. B. Kemper, D. Carl, J. Schnekenburger, I. Bredebusch, M. Schäfer, W. Domschke, G. von Bally (2006) Investigation of living pancreas tumor cells by digital holographic microscopy, *J. Biomed. Opt.* **11**: 034005
21. P. Ferraro, G. Coppola, S. De Nicola, A. Finizio, G. Pierattini (2003) Digital holographic microscope with automatic focus tracking by detecting sample displacement in real time, *Opt. Lett.* **28**: 1257-1259
22. M. Liebling, M. Unser (2004) Autofocus for digital Fresnel holograms by use of a Fresnelet-sparsity criterion, *J. Opt. Soc. Am.* A **21**: 2424–2430
23. F. Dubois, C. Schockaert, N. Callens, C. Yourassowsky (2006) Focus plane detection criteria in digital holography microscopy by amplitude analysis, *Opt. Express.* **14**: 5895–5908
24. P. Langehanenberg, B. Kemper, G. von Bally (2007) Autofocus algorithms for digital-holographic microscopy, *Proc. SPIE* 6633, 66330E
25. W. Li, N. C. Loomis, Q. Hu, C. S. Davis (2007) Focus detection, from digital in-line holograms based on spectral l1 norms, *J. Opt. Soc. Am. A* **24**: 3054–3062

26. P. Langehanenberg, B. Kemper, D. Dirksen, G. von Bally (2008) Autofocusing in digital holographic phase contrast microscopy on pure phase objects for live cell imaging, *Appl. Opt.* **47**: D176–D182
27. Y. Yang, B. Kang, Y. Choo (2008) Application of the correlation coefficient method for determination of the focal plane to digital particle holography, *Appl. Opt.* **47**: 817-824
28. M. L. Tachiki, M. Itoh, T. Yatagai (2008) Simultaneous depth determination of multiple objects by focus analysis in digital holography, *Appl. Opt.* **47**: D144-D153
29. F. Dubois, C. Yourassowsky, O. Monnom, J.-C. Legros (2006) Digital holographic microscopy for the three-dimensional dynamic analysis of in vitro cancer cell migration, *J. Biomed. Opt.* **11**: 054032
30. P. Langehanenberg, L. Ivanova, I. Bernhardt, S. Ketelhut, A. Vollmer, D. Dirksen, G. Georgiev, G. von Bally, B. Kemper (2009) Automated three-dimensional tracking of living cells by digital holographic microscopy, *J. Biomed. Opt.* **14**: 014018
31. U. Schnars, W. Jüptner (2002) Digital recording and numerical reconstruction of holograms, *Meas. Sci. Technol.* **13**: R85– R101
32. L. Yaroslavsky (2004) Digital Holography and Digital Image Processing: Principles, Methods, *Algorithms, Kluwer Academic Publishers*
33. T. Kreis (2005) Handbook of Holographic Interferometry: Optical and Digital Methods, *Wiley-VCH*
34. M.K. Kim, L. Yu, C.J. Mann (2006) Interference techniques in digital holography, *J. Opt. A* **8**: S518-523
35. T.-C. Poon (2006) Digital Holography and Three-Dimensional Display, *Springer*
36. M. Liebling, T. Blu, M. Unser (2004) Complex-wave retrieval from a single off-axis hologram, *J. Opt. Soc. Am.* A **21**: 367– 377
37. B. Kemper, D. Carl, J. Schnekenburger, I. Bredebusch, M. Schäfer, W. Domschke, G. von Bally (2006) Investigation of living pancreas tumor cells by digital holographic microscopy, *J. Biomed. Opt.* **11**: 034005
38. T. Colomb, F. Montfort, C. Depeursinge (2008) Small Reconstruction Distance in Convolution Formalism, in Digital Holography and Three-Dimensional Imaging, *OSA Technical Digest (Optical Society of America)*, paper DMA4
39. T. Kreis (1996) Holographic Interferometry: Principles and Methods, *Akademie Publishing*
40. P. Marquet, B. Rappaz, F. Charrière, Y. Emery, C. Depeursinge, P. Magistretti (2007) Analysis of cellular structure and dynamics with digital holographic microscopy, *Proc SPIE* 6633, 66330F
41. G. Nomarski (1955) Differential microinterferometer with polarized waves, *J. Phys. Radium.* **16**: 9-13
42. Y. Sun, S. Duthaler, B. J. Nelson (2004) Autofocusing in computer microscopy: selecting the optimal focus algorithm, *Microsc. Res. Tech.* **65**: 139–149
43. F. C. Groen, I. T. Young, G. Ligthart (1985) A comparison of different focus functions for use in autofocus algorithms, *Cytometry* **6**: 81–91
44. L. Firestone, K. Cook, K. Culp, N. Talsania, K. Preston Jr (1991) Comparison of autofocus methods for automated microscopy, *Cytometry* **12**: 195–206
45. M. Bravo-Zanoguera, B. v. Massenbach, A. L. Kellner, J. H. Price (1998) High-performance autofocus circuit for biological microscopy, *Rev. Sci. Instrum.* **69**: 3966–3977
46. J. He, R. Zhou, Z. Hong (2003) Modified fast climbing search auto-focus algorithm with adaptive step size searching technique for digital camera, *IEEE Transactions on Consumer Electronics* **49**: 257-262
47. B. Kemper, D. Carl, A. Höink, G. von Bally, I. Bredebusch, J. Schnekenburger (2006) Modular digital holographic microscopy system for marker free quantitative phase contrast imaging of living cells, *Proc. SPIE* 6191, 61910T
48. M. Bielaszewska, A. Bauwens, L. Greune, B. Kemper, U. Dobrindt, J. M. Geelen, K. S. Kim, A. Schmidt, H. Karch (2009) Vacuolization of human microvascular endothelial cells by enterohaemorrhagic Escherichia coli, *Thrombosis and Haemostasis* **102**: 1080-1092
49. B. Kemper, S. Kosmeier, P. Langehanenberg, G. von Bally, I. Bredebusch, W. Domschke, J. Schnekenburger (2007) Integral refractive index determination of living suspension cells by multifocus digital holographic phase contrast microscopy, *J. Biomed. Opt.* **12**: 054009
50. B. Kemper, P. Langehanenberg, Gert von Bally (2007) Methods and applications for marker-free quantitative digital holographic phase contrast imaging in life cell analysis, *Proc. SPIE* 6796, 67960E
51. B. Kemper, S. Kosmeier, P. Langehanenberg, S. Przibilla, C. Remmersmann, S. Stürwald, G. von Bally (2009) Application of 3D tracking, LED illumination and multi-wavelength techniques for quantitative cell analysis in digital holographic microscopy, *Proc SPIE* 7184, 71840R
52. B. Kemper, A. Bauwens, A. Vollmer, S. Ketelhut, P. Langehanenberg, J. Müthing, H. Karch, G. von Bally (2010) Label-free Quantitative Cell Division Monitoring of Endothelial Cells by Digital Holographic Microscopy, *J. Biomed. Opt.* **15**: 036009
53. B. Kemper, P. Langehanenberg, A. Vollmer, S. Ketelhut, G. von Bally (2010) Digital Holographic Microscopy - Label-free 3D Migration Monitoring of Living Cells, *Imaging and Microscopy.* **4**: 26-28